Synthetic Aperture Focusing of Ultrasonic Data from Multilayered Media Using an Omega-K Algorithm

Martin H. Skjelvareid, Tomas Olofsson, Yngve Birkelund and Yngvar Larsen

***Abstract*—The synthetic aperture focusing technique (SAFT) is used to create focused images from ultrasound scans. SAFT has traditionally been applied only for imaging in a single medium, but the recently introduced Phase Shift Migration (PSM) algorithm has expanded the use of SAFT to multilayer structures. In this article we present a similar focusing algorithm called MULOK (MUlti-Layer Omega-K), which combines PSM and the ω–k algorithm to perform multilayer imaging more efficiently. The asymptotic complexity is shown to be lower for MULOK than for PSM, and this is confirmed by comparing execution times for implementations of both algorithms. To facilitate the complexity analysis, a detailed description of algorithm implementation is included, which also serves as a guide for readers interested in practical implementation. Using data from an experiment with a water-plexiglas-aluminium structure, we show that there is essentially no difference in image quality between the two algorithms.**

I. Introduction

Synthetic aperture as a concept is used within both radar, sonar, seismic and ultrasound imaging. The technique is based on emitting a wave into a region of interest, recording the backscattered echoes, and repeating this for several positions. Recorded data are subsequently combined to create a large synthetic aperture, yielding a high-resolution image of the reflectivity in the region.

Within the field of seismic imaging, synthetic aperture techniques are known as migration techniques. Computer-based processing of seismic data started in the 1970s [1], and the initial methods were limited to time-space domain processing. In 1978, Stolt [2] introduced what is now called the frequency-wavenumber, or $\omega-k$, algorithm, performing all processing in the temporal and spatial frequency domain. This approach proved to be significantly faster than the other methods available at the time, and it has since become widely used in many related fields. Its main disadvantage is that it requires the wave velocity of the propagating medium to be constant. In the same year, Gazdag [3] introduced the Phase Shift Migration (PSM) algorithm, which also operates in the frequency-wavenumber domain. Although not as fast as the $\omega-k$ algorithm, it allows the wave velocity to vary with depth.

Both the $\omega-k$ and the PSM algorithm are based on extrapolating the backscattered wavefield from the plane in which it is recorded, and down into the region to be imaged. In Fourier analysis of wave fields this is also known as angular spectrum propagation [4], [5].

Building on previous work within sonar and radar imaging, synthetic aperture focusing was introduced to the field of NDT ultrasonics in the 1970s, and came to be known as the Synthetic Aperture Focusing Technique (SAFT) [6]. Although the time-domain delay-and-sum method was the starting point, frequency domain algorithms were soon adopted by the ultrasonic community [7], [8], [9], [10], [11], and in recent years there has also been a growing interest in adapting such algorithms for arrays [12], [13]. Researchers have mainly focused on imaging in a single, constant-velocity medium, but some time-domain methods for multilayer structures have been developed [14], [15], and recently Olofsson [16] introduced the use of the frequency-domain PSM algorithm for processing multilayer data.

There are several applications for ultrasound imaging of multilayer structures. One very important case is that of immersion scans, in which an object is immersed in water and a number of pulse-echo measurements are performed by scanning the transducer in the water layer above the object. The main advantages of immersion scans, as opposed to contact scans, are that the water layer acts as a good and uniform couplant for the acoustic waves, and that there is no friction causing transducer wear. The transducer used in immersion scans is usually geometrically focused to provide a good lateral resolution in the transducer focal zone. Synthetic aperture techniques represent an alternative that can be used to obtain a high lateral resolution that is independent of depth.

As previously mentioned, the ω–k algorithm has proven to be very efficient for single-layer processing, while the PSM algorithm is capable of imaging structures where the wave velocity varies with depth. In 1989, Kim [17] introduced a method for seismic imaging which combines the advantages of both algorithms. He assumed that the geological structure of the earth can be approximated as a finite number of layers with constant wave velocity and used the PSM algorithm to extrapolate the wavefield down to the interfaces between the layers. He then used the $\omega-k$ algorithm to effectively image the interior of each layer. In this paper, we demonstrate that the same approach can be used for ultrasonic imaging of multilayer structures, and we will refer to this as the MUlti-Layer Omega-K algorithm (MULOK). The algorithm is compared to the PSM algorithm in terms of both computational complexity and image quality.

To simplify the treatment of the algorithms, a two-

The authors would like to thank Breivoll Inspection Technologies and the Research Council of Norway for funding this work.

dimensional geometry is considered here, but an extension to three dimensions is straightforward. A real ultrasound application is usually three-dimensional by its own nature, but if the region of interest is homogenous along one direction, a two-dimentional approximation can be made without any loss of information.

In order to compare the asymptotical complexity of the PSM and MULOK algorithms, a detailed description of the algorithm implementations has been included. As an added benefit, the description also serves as a guide for practical implementation.

The remainder of this article is organized as follows: In Section II, the theory of the PSM and MULOK algorithms is presented, and in Section III, the asymptotic complexity of each algorithm is analyzed and compared with actual execution times. An experiment illustrating the imaging performance of both algorithms is presented in Section IV, before we state our conclusions in Section V. Details of algorithm implementation and complexity analysis have been placed in appendices A-E to maintain the flow of the article for the general reader.

II. Theory

A. The exploding reflector model

Derivation of migration algorithms for the monostatic case are often based on the exploding reflector model [18], [19], which simplifies the inverse imaging problem. It reduces the two-way pulse-echo scenario to a one-way scenario where we assume that the scatterers themselves are sources of acoustic energy.

Figure 1(a) illustrates a B-scan of a two-layer geometry, where a transducer is scanned along the x axis and a pulse-echo measurement is performed for each x position. A scatterer is present in the second layer, and because the two layers have different wave velocities, both the transmitted and the reflected wave is refracted at the interface between the layers.

Figure 1(b) shows how the exploding reflector model is applied to the same geometry. The scatterer explodes and creates a wave which travels towards an array of transducer positions, undergoing the same refraction as for the pulse-echo case. In order for the time delay of the pulses to remain the same under the exploding reflector model as for the actual pulse-echo measurement, an effective wave velocity of half the actual velocity must be assumed,

$$\hat{c}_l = \frac{c_l}{2}, \tag{1}$$

where l is the layer index. The model is general and can be applied for an arbitrary number of layers.

In most ultrasonic measurements, there are multiple reflectors, and the wave field measured by the transducer is then approximated as a superposition of waves from several exploding reflectors. This assumption holds as long as multiple reflections between scatterers can be neglected.

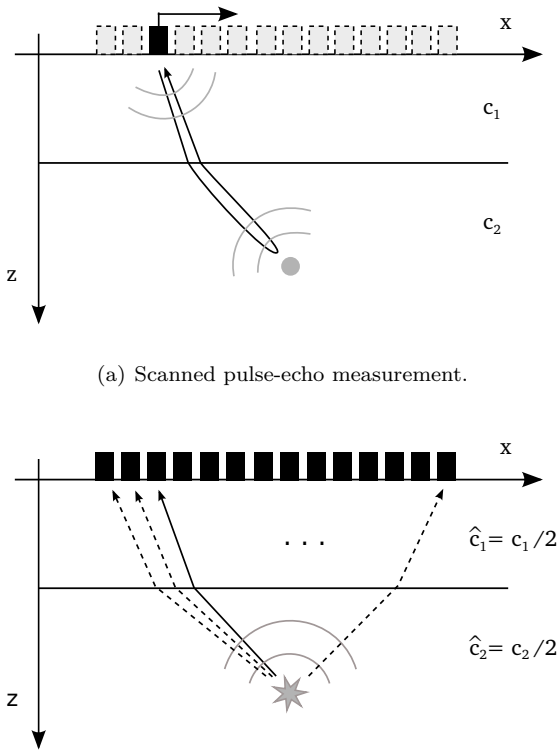

(a) Scanned pulse-echo measurement.

(b) Exploding reflector model.

Figure 1: Pulse-echo measurements and exploding reflector model.

B. Extrapolation of wave field in Fourier domain

For migration algorithms, the purpose of wave field extrapolation is to calculate the wave field at an arbitrary depth from measurements performed at a given depth, here denoted by Z. In the following derivation we will assume that all scatterers are located in the half-space $z > Z$.

Let $p(t, x, z)$ denote the wave field generated by a set of exploding reflectors. The wave field has to obey the scalar wave equation

$$\left[\frac{\partial^2}{\partial x^2} + \frac{\partial^2}{\partial z^2} - \frac{1}{\hat{c}^2}\frac{\partial^2}{\partial t^2}\right] p(t, x, z) = 0, \tag{2}$$

where the sound speed $\hat{c} = c/2$ is used because the exploding reflector model is assumed. Solutions to the wave equation are in the form of plane harmonic waves,

$$p(t, x, z) = Pe^{i(k_x x + k_z z - \omega t)}, \tag{3}$$

where ω is the angular frequency, k_x and k_z are the horizontal and vertical wavenumbers, and P is the complex amplitude for the plane wave. Applying Eq. (2) to Eq. (3), we find that ω, k_x and k_z are related through the equation

$$\frac{\omega^2}{\hat{c}^2} = k_x^2 + k_z^2. \tag{4}$$

If ω is positive, a harmonic plane wave travels in the direction of the wavenumber vector $[k_x, k_z]$ as time increases. If ω is negative, the wave travels in the opposite

direction. Since the wave field is measured at $z = Z$, and all scatterers are located in the half-space $z > Z$, all recorded waves are travelling in the negative z direction. We can also see from Eq. (4) that only two of the three variables ω, k_x and k_z are independent. Choosing k_z as the dependent variable, we rearrange Eq. (4) to obtain

$$k_z(\omega, k_x) = -\text{sgn}(\omega) \cdot \sqrt{\frac{\omega^2}{\hat{c}^2} - k_x^2}, \tag{5}$$

where the sign function ensures that the k_z value represents an upgoing wave.

The general solution for an arbitrary wave field can be expressed as a sum of plane waves of the form given in Eq. (3),

$$p(t, x, z) = \iint_{-\infty}^{\infty} P(\omega, k_x) e^{i(k_x x + k_z(\omega, k_x) z - \omega t)} \, dk_x \, d\omega, \tag{6}$$

where $P(\omega, k_x)$ denotes the complex amplitude for the independent pair (ω, k_x). Defining

$$P(\omega, k_x, z) \equiv P(\omega, k_x) e^{ik_z(\omega, k_x) z}, \tag{7}$$

we can rewrite Eq. (6) as

$$p(t, x, z) = \iint_{-\infty}^{\infty} P(\omega, k_x, z) e^{i(k_x x - \omega t)} \, dk_x \, d\omega. \tag{8}$$

Equation (8) represents an inverse Fourier transform of $P(\omega, k_x, z)$ from coordinates (ω, k_x) to (t, x). The corresponding forward transform is given by

$$P(\omega, k_x, z) = \frac{1}{4\pi^2} \iint_{-\infty}^{\infty} p(t, x, z) e^{-i(k_x x - \omega t)} \, dx \, dt, \tag{9}$$

where $1/(4\pi^2)$ is a normalization constant. Thus, $P(\omega, k_x, z)$ is the Fourier transform of the wavefield in the x plane at depth z. Let $P(\omega, k_x, Z)$ denote the Fourier transform of the wavefield recorded at depth Z. Inserting this into Eq. (7) and solving for $P(\omega, k_x)$, we get that

$$P(\omega, k_x, z) = P(\omega, k_x, Z) e^{ik_z(z - Z)}, \tag{10}$$

where the explicit dependency of k_z on ω and k_x has been omitted for ease of notation. Defining Δz as the offset $z - Z$, and inserting Eq. (10) into Eq. (8), we obtain a general expression for wave field extrapolation,

$$p(t, x, Z + \Delta z) = \iint_{-\infty}^{\infty} P(\omega, k_x, Z) e^{ik_z \Delta z} \, e^{i(k_x x - \omega t)} \, dk_x \, d\omega. \tag{11}$$

C. Imaging condition

Given an expression for the wave field $p(t, x, z)$, an *imaging condition* is needed to obtain an image $I(x, z)$ of the exploding reflectors. For the exploding reflector model, the imaging condition is to set $t = 0$ [19], so that

$$I(x, z) = p(t{=}0, x, z). \tag{12}$$

The wave field emitted from a scatterer is maximally concentrated in space at the time of explosion (t=0), and thus the above imaging condition is chosen to produce a maximally focused image.

D. Imaging using Phase Shift Migration

Applying the imaging condition of Eq. (12) to Eq. (11), we get the following expression:

$$I(x, Z{+}\Delta z) = \iint_{-\infty}^{\infty} P(\omega, k_x, Z) e^{ik_z \Delta z} e^{ik_x x} \, dk_x d\omega. \tag{13}$$

Note that inserting $t = 0$ into Eq. (11) reduces the inverse transform with respect to ω to a simple integral over ω. Eq. (13) can be used iteratively to create an image line by line, by applying it for all depths $Z{+}\Delta z$ to be imaged. In seismic processing, this is called Phase Shift Migration (PSM), referring to the phase shift given by the term $e^{ik_z \Delta z}$.

E. Imaging through Stolt transform

Equation (13) is very similar to an inverse Fourier transform of $P(\omega, k_x, Z)$, but it has an $e^{ik_z \Delta z}$ kernel rather than an $e^{-i\omega t}$ kernel. It can be recast into a proper inverse Fourier transform by a change of variables from ω to k_z. Integrals in the form of Fourier transforms are of particular interest, as they can be calculated using the computationally efficient Fast Fourier Transform (FFT) and its inverse counterpart (IFFT).

We obtain an expression for ω by using the relation given in Eq. (4), and assuming, as in Section II-B, that ω and k_z have opposite signs, so that

$$\omega(k_z, k_x) = -\text{sgn}(k_z) \cdot \hat{c} \sqrt{k_x^2 + k_z^2}. \tag{14}$$

By substituting Eq. (14) into Eq. (13), we get

$$I(x, Z{+}\Delta z) = \iint_{-\infty}^{\infty} P(k_z, k_x, Z) e^{ik_z \Delta z} e^{ik_x x} \, dk_x dk_z, \tag{15}$$

where

$$P(k_z, k_x, Z) = A(k_z, k_x) \cdot P(\omega(k_x, k_z), k_x, Z), \tag{16}$$

and

$$A(k_z, k_x) = \frac{\partial \omega(k_z, k_x)}{\partial k_z} = \frac{\hat{c}}{\sqrt{1 + \frac{k_x^2}{k_z^2}}}. \tag{17}$$

We see here that relative to the original wave field $P(\omega, k_x, Z)$, the substitution of variables leads to a multiplication with an amplitude factor $A(k_z, k_x)$ and a shift in ω given by $\omega(k_z, k_x)$.

F. Adaptation to multilayer case

Assume now that we have several layers with potentially different wave velocities, as illustrated in Fig. 2. Let the layers be numbered with $l = 1, 2, ..., L$, and let d_l and c_l denote the thickness and wave velocity of layer l. The top of the uppermost layer is denoted by Z_1, and the interfaces

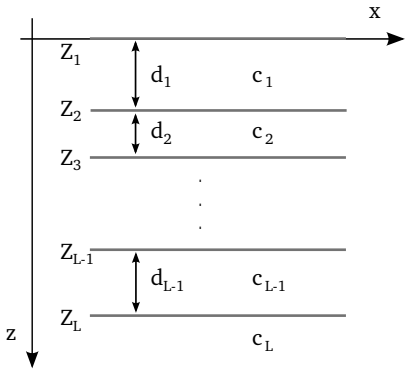

Figure 2: Illustration of horisontally layered geometry

between the layers are denoted by Z_l, so that the top of layer l is given by $Z_l = Z_1 + \sum_{m=1}^{l-1} d_m$.

We know from Eq. (10) that in a medium with constant sound speed, the wave field $P(\omega, k_x, z)$ can be calculated by multiplying a reference wave field $P(\omega, k_x, Z)$ with a phase factor $e^{ik_z \Delta z}$. In the multilayer case, the field cannot be extrapolated through several layers directly, since k_z is a function of the medium velocity $\hat{c}_l$,

$$k_{zl} = -\text{sgn}(\omega) \cdot \sqrt{\frac{\omega^2}{\hat{c}_l^2} - k_x^2}, \tag{18}$$

where the layer dependence is indicated by index l. However, extrapolation within each layer is still possible,

$$P(\omega, k_x, Z_l + \Delta z) = P(\omega, k_x, Z_l) \cdot e^{ik_{zl}\Delta z}, \ \Delta z < d_l, \tag{19}$$

where $P(\omega, k_x, Z_l)$ denotes the field at interface Z_l, and $P(\omega, k_x, Z_l + \Delta z)$ denotes the field at depth $z = Z_l + \Delta z$.

If the wave field is to be extrapolated to more than one layer, the transmission of waves through the layer interfaces has to be considered. The transmission factor between different media is generally a complex function, dependent on both incident angle and the acoustic impedances of the media [20]. However, for most commonly available ultrasound transducers, the directivity of the transducer limits the emitted and received wave fields to a relatively small angle interval. We will therefore assume that the transmission factors are approximately independent of incident angle, so that the wave fields directly above and directly below an interface are proportional;

$$P(\omega, k_x, Z_l^-) \propto P(\omega, k_x, Z_l^+), \tag{20}$$

where the plus and minus signs are used to indicate the upper and lower side of the interface, respectively. Since we are mainly interested in relative amplitudes within each layer, the amplitude scaling effect imposed by the interfaces is here considered to be unimportant to the imaging problem.

Assuming proportonality across interfaces, the wave field at an arbitrary interface Z_l can, within a scaling factor, be calculated from the wave field measured at Z_1,

$$P(\omega, k_x, Z_l) \propto P(\omega, k_x, Z_1) \cdot e^{\,i \sum_{m=1}^{l} k_{zm} d_m}. \tag{21}$$

The equations (19) and (21) constitute the basis for PSM imaging of several layers. The imaging procedure for layer l can be summarized as follows:

1) Calculate the wave field at the top of the layer interface, $P(\omega, k_x, Z_l)$, using Eq. (21)
2) For each depth Δz to be imaged within the layer:
   a) Shift the wave field downwards with Δz by multiplying with a phase factor, according to Eq. (19), to obtain $P(\omega, k_x, Z_l + \Delta z)$
   b) Create an image line $I(x, Z_l + \Delta z)$ by integrating with regard to ω and inverse transforming with regard to k_x, according to Eq. (13).

Instead of creating an image of each layer line by line, the Stolt transform introduced in Section II-E can be adapted to the multilayer case, to enable imaging of an entire layer through a single inverse Fourier transform. This approach is what we call the Multi-Layer Omega-K algorithm (MULOK). The complete image for layer l is then given by

$$I_l(x, \Delta z) = \iint_{-\infty}^{\infty} P(k_z, k_x, Z_l) e^{-ik_z \Delta z} e^{ik_x x} \, dk_x dk_z, \ \Delta z < d_l, \tag{22}$$

where

$$P(k_z, k_x, Z_l) = A_l(k_z, k_x) \cdot P_l(\omega_l(k_x, k_z), k_x, Z_l), \tag{23}$$

$$A_l(k_z, k_x) = \frac{\hat{c}_l}{\sqrt{1 + \frac{k_x^2}{k_{zl}^2}}}, \text{ and} \tag{24}$$

$$\omega_l(k_z, k_x) = -\text{sgn}(k_{zl}) \cdot \hat{c}_l \sqrt{k_x^2 + k_{zl}^2}. \tag{25}$$

The imaging procedure to create an image of layer l can be summarized in the following way:

1) Calculate the wave field at the top of the layer, $P(\omega, k_x, Z_l)$, using Eq. (21)
2) Use Eq. (23) – (25) to perform the variable transformation from ω to k_{zl}.
3) Inverse transform to obtain the image within the layer, $I_l(x, \Delta z)$, using Eq. (22)

G. Comments on theoretical resolution

The lateral resolution of an synthetic aperture image is dependent on the bandwidth of the k_x spectrum [21], and this bandwidth is limited by the effective length L of the transducer. A common rule of thumb for the single-layer case is that this makes the maximum lateral resolution approximately $L/2$ [11]. Here we will argue that this limit is also relevant for the multilayer case.

According to Snell's law, the k_x wavenumber of a wave incident on a layer interface must remain the same after transmission into the next medium. Thus, the refraction of the wave does not in itself alter the horizontal

wavenumber, but the transmission factors between media are generally dependent on incident angle, making the interface a filter for the k_x spectrum. The bandwidth of the k_x spectrum is only maintained as long as the transmission factors are approximately uniform within the divergence angle of the transducer, but in practice, this requirement is fulfilled for many transducer designs and material combinations of interest. For example, for a immersion scan of copper using a 2.25 MHz 10 mm diameter transducer, the echo transmission factor varies by only approximately 6% within the transducer beam [16]. As long as the k_x spectrum bandwidth can be assumed to be the same for the single-layer and multilayer case, the theoretical lateral resolution of $L/2$ is also the same.

III. Algorithmic complexity

A. Aymptotic complexity

The effectiveness of an algorithm is often quantified by analyzing how the number of operations grow as the size of the input data tends towards infinity, and this asymptotic complexity is denoted using Big O notation. In the case of the PSM and MULOK algorithms, the size of the input data is given by the number of time samples, N, the number of measurement positions, M, and the number of layers, L.

The asymptotic complexities for each individual step of the algorithms are analyzed in appendix E, and listed in tables II and III. The overall complexity of each algorithm is given by the algorithm step with the highest order complexity. To analyze this, we consider the complexities with regard to N, M and L separately, assuming that the two remaining variables are kept constant. The highest order complexities are summarized in Table I. MULOK is seen to have a lower complexity than PSM with regard to N, since $N \log N < N^2$, while the complexity with regard to M and L is the same for both algorithms.

Algorithm	N	M	L
PSM	$O(N^2)$	$O(M \log M)$	$O(L)$
MULOK	$O(N \log N)$	$O(M \log M)$	$O(L)$

Table I: Asymptothic complexities PSM and MULOK, regarding N, M and L separately.

B. Empirical evaluation of execution times

To do a realistic comparison of the two algorithms, a number of simulated processings were performed in Matlab. Matrices with random numbers were used instead of ultrasonic scans. The number of measurement positions, M, was set to 128, and the processing times were measured for different number of time samples, N. The simulations were performed on a dual-core 2 GHz laptop with 2 GB RAM, running a 64-bit Linux version of Matlab R2009b

The resulting execution times are plotted in Fig. 3. Note that both the x and the y axes of the plots are logarithmic. Figures 3(a) and 3(b) show the execution times as function of N when the number of layers L is 2 and 5, respectively. To compare the asymptotic complexities with the execution times of the simulation, lines corresponding to N^2 and $N \log N$ have been added to the plot, normalized to intersect with the execution time for the highest value of N.

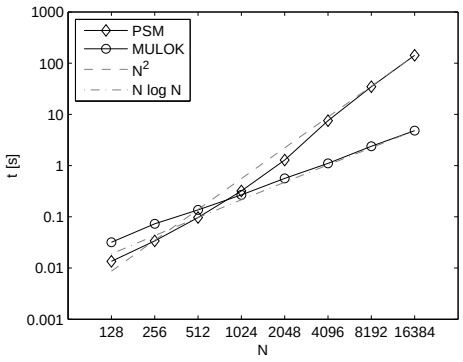

(a) L=2, M=128

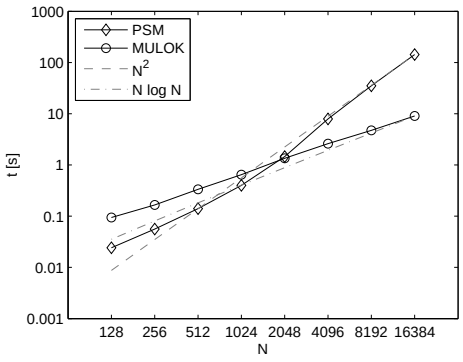

(b) L=5, M=128

Figure 3: Execution time simulation results.

We find from figures 3(a) and 3(b) that PSM has a lower execution time than MULOK for small N, but that MULOK is much faster as N grows larger. For example, for $L = 5$ and $N = 16384$, MULOK is approximately 15 times faster than PSM, and for $L = 2$ and $N = 16384$, MULOK is approximately 30 times faster. Comparing the results for $L = 2$ and $L = 5$, we see that the execution time of the PSM algorithm is approximately the same for both cases, while the time for the MULOK algorithm is significantly higher for $L = 5$. Thus, a higher number of layers shifts the crossover point between the algorithms to a higher N value. The reason that MULOK is more heavily influenced by L than PSM can be found by comparing the complexities for each algorithmic step, listed in Table II and Table III. PSM has only one step whose complexity is proportional to L, while almost all steps in MULOK are have complexities proportional to L.

The exection times are seen to correspond well to the asymptotic complexities indicated by the dashed lines, particularly as N grows larger. This indicates that the general trends seen here can be assumed to be valid in general, even if the given execution times presented here are valid only for one specific implementation of the algorithms.

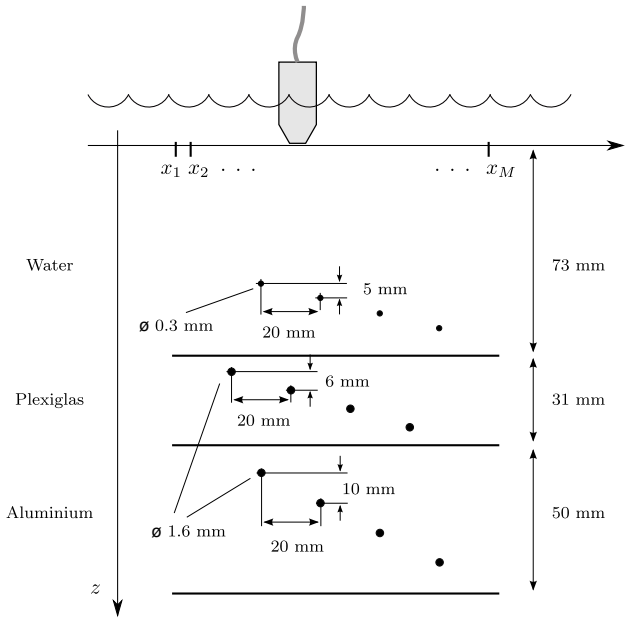

Figure 4: Experiment setup

IV. Experiment

In Section III it was shown that the asymptotical complexity of MULOK is lower than that of PSM with regard to N. To validate that MULOK is also capable of producing the same image quality as PSM, an experiment with a three-layer structure was conducted.

Two test blocks with side-drilled holes were placed on top of each other and immersed in a water tank, and an array of four steel pins was placed over the two blocks, as shown in Fig. **??**. A B-scan of the arrangement was performed using a 2.25 MHz transducer with 6 mm diameter, moved in steps of 1 mm, with a sampling frequency of 12.5 MHz. N = 1040 time samples were recorded in each of the M = 111 measurement positions.

The upper and lower block consisted of plexiglas and aluminium, and were 31 and 50 mm thick, respectively. Each of the blocks had four side-drilled holes, which were all 1.6 mm in diameter and 30 mm deep. The vertical spacing between the holes was 6 mm in the plexiglas block and 10 mm in the aluminium block, while the horizontal spacing was 20 mm for both blocks. The blocks were also shifted horizontally approximately 10 mm, so that the upper holes would not create a dominating "shadow" for the lower holes. The steel pins were 0.3 mm in diameter, with a vertical spacing of 5 mm and a horizontal spacing of 20 mm. The scan line was centered over the holes and pins in the y direction.

To compensate for limited dynamic range in the ultrasonic aquisition system, a time-dependent damping/amplification was applied during the scan. The water-plexiglas interface echo was damped -10 dB, and the echoes from the aluminium layer were amplified by +20 dB.

The envelope of the B-scan was calculated using the Hilbert transform, and the resulting raw data image is shown in the two leftmost plots of Fig. 5, plotted with both a 25 dB and a 50 dB dynamic range. Two different dynamic ranges were used emphasize the difference between high-amplitude and low-amplitude effects. The front echo from the water-plexiglas interface is seen as a horizontal line at approximately 100 μs, and echoes from the plexiglas-aluminium and the aluminium-water interfaces are visible at approximately 123 and 137 μs, respectively.

The wave velocity for water, plexiglas and aluminium is approximately 1480 m/s, 2730 m/s and 6320 m/s, and the difference in velocity can be seen clearly in the B-scan, as the appearent thickness of the layers on the time axis is far from their actual thickness. The echoes from the steel pins and the side-drilled holes are seen as four reflections in each of the layers, and the width of the reflections increases with depth because of the divergence of the emitted transducer pulse. There are also some weaker reflections cluttering the image in both the plexiglas and aluminium layers. These are caused by multiple reflections of the scattterers.

The raw data was processed with both the MULOK and the PSM algorithms, and the resulting images are shown in Fig. 5, plotted with absolute value on a dB intensity scale. Like the raw data, the images are shown with both 25 dB and 50 dB dynamic ranges.

Although there are some slight differences between the PSM and MULOK images, these differences are very low in amplitude, and the overall impression is that the two images are visually identical. This indicates that for practical purposes, PSM and MULOK will be equvivalent in terms of image quality.

The reflections from the scatterers have been focused, resulting in an improved lateral horizontal resolution that is approximately the same for all scatterers, independent of depth or layer. Multiple reflections have been partially focused or defocused, depending on how close they are in time to their original scatterers. For example, the reflection seen at approximately t = 130 μs, x = 30 mm in the raw data appears to be caused by a scatterer in the aluminium layer, but it is actually a multiple reflection of the leftmost scatterer in the water layer. In the focused images, the reflection has been defocused into a curve, since it did not originate in the aluminium layer.

The improvement in lateral resolution can be seen more clearly in Fig. 6, which shows the raw data and MULOK focused image for the rightmost scatterer in each layer. The -6dB width of the response from each scatterer was found, after interpolation to finer x resolution, to be approximately 3 mm, 3 mm and 3.6 mm, from top to bottom. This corresponds quite well to the theoretical resolution of approximately half the transducer diameter, indicating that the assumptions discussed in Section II-G are valid in this case.

V. Discussion and conclusions

We have presented a new algorithm for processing of ultrasonic data from multilayer structures, called MULOK, and compared it with the PSM algorithm. Both algorithms represent an extension of the SAFT concept to the case

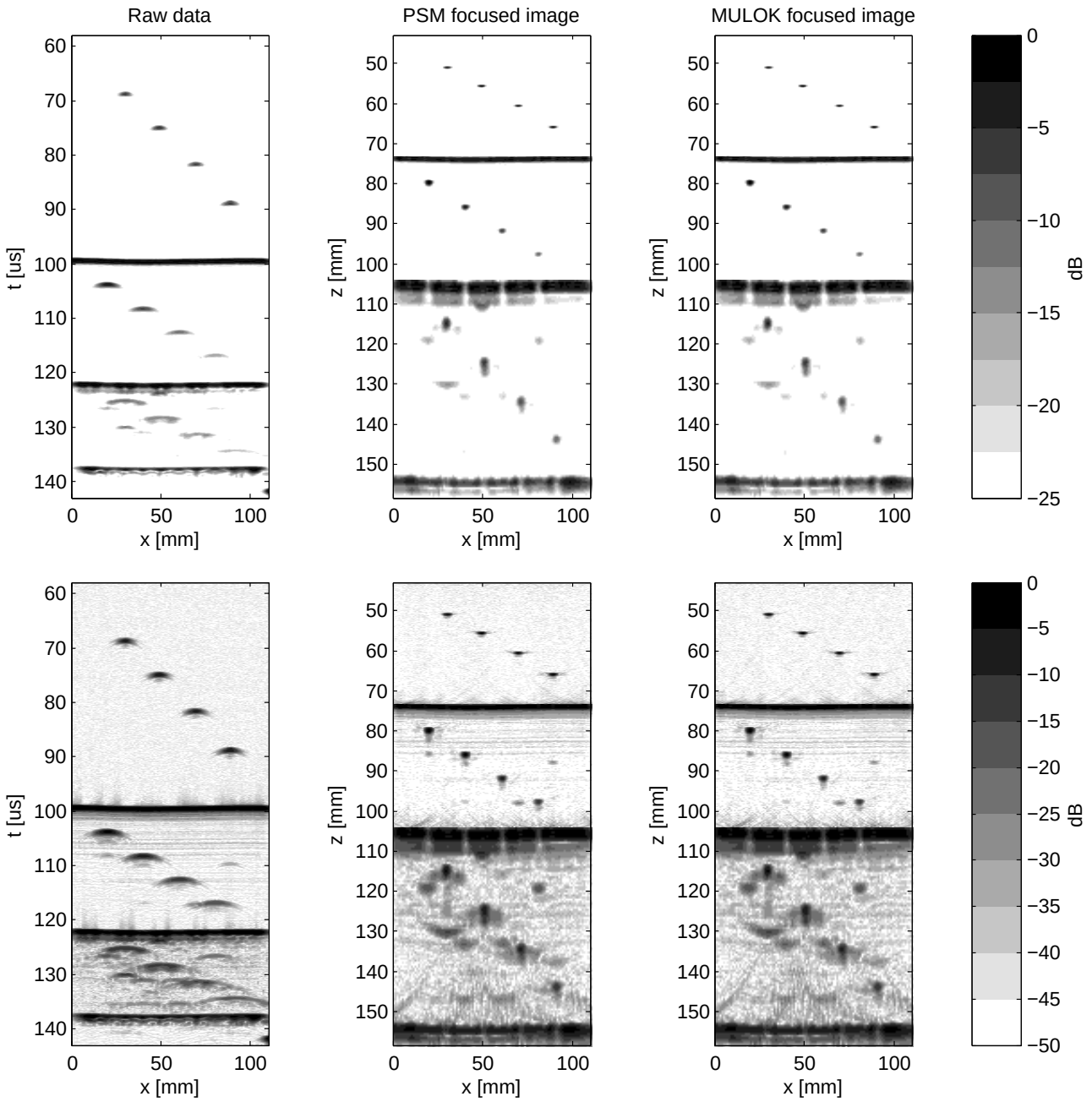

Figure 5: Comparison of raw data and images focused by PSM and MULOK, displayed on a dB intensity scale. The dynamic range of the top and bottom row is 25 and 50 dB, respectively.

where the imaged geometry consists of layers with differing wave velocities.

In theory, the algorithms can focus through an arbitrary number of layers. However, since the transmission factor between layers is generally lower than one, both the transmitted pulse and the backscattered echo will be significantly damped at each interface. Thus, the signal-to-noise ratio is likely to limit the number of layers that can be imaged in practice. In addition, multiple reflections from within the first layers may interfere with echoes from layers further down.

We have shown, both theoretically and by numerical simulation, that the MULOK algorithm has a lower asymptotic complexity than the PSM algorithm. However, the simulations also indicated that the effectiveness of the MULOK algorithm decreases as the number of layers increases, while the execution time of the PSM algorithm is more or less independent of number of layers.

We have also demonstrated that the image quality and lateral resolution is approximately the same for both algorithms. Note however that if the interpolation step of the MULOK algorithm is not performed accurately enough, the focused image will contain visible artefacts. Thus, the accuracy of the interpolation should be adjusted according to the image quality required. There are also variations of the $\omega - k$ algorithm which do an approximate but

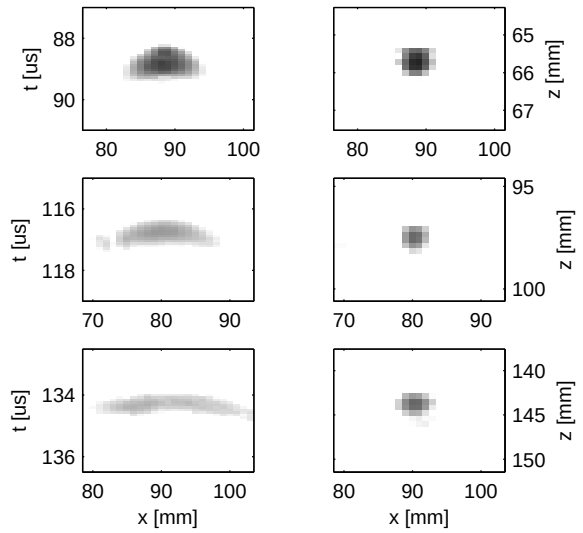

Figure 6: Zoomed-in plot of rightmost scatterers in each layer. Raw data in left column, focused image in right. The -6dB width of the focused scatterers is, from top to bottom, 3 mm, 3 mm, and 3.6 mm.

efficient mapping from ω to k_z without any interpolation, for example using the chirp z-transform [22]. Modifying MULOK to accommodate such methods is seen as a subject for future work.

Taking all factors into account, we see that the choice between PSM and MULOK relies both on the geometry to be imaged and the resources available for implementation. If the number of input samples is relatively large, the number of layers is low, and the interpolation between ω and k_z can be executed efficiently and accurately, MULOK can produce the same image quality as PSM in a much more efficient manner. If these requirements are not fulfilled, PSM may be a better alternative.

Appendix

A. Matrix representation of discrete data

In Section II, the theory was outlined for the case of continuous signals, and it was also assumed that wavefield in the measurement plane is known for all x and t. In practice, the boundary condition must be sampled discretely both in time and space, for a finite time period and over a finite section of the x axis.

We assume that each measurement position, a pulse is emitted, and N_t time samples are recorded, corresponding to time instants $t_1, t_2, \ldots, t_{N_t}$. The measurement is performed at M different x positions, $x_1, x_2, \ldots, x_M$. Time samples are equally spaced with $\Delta T = 1/f_s$, where f_s is the sampling frequency, and the x positions are equally spaced with ΔX. Assuming that the measurement is done at depth Z_1, the discrete data set can be organized in a matrix $\boldsymbol{P}_{tx}[Z_1]$, with element p_{ij} corresponding to time instant t_i of the pulse-echo measurement at position x_j:

$$\boldsymbol{P}_{tx}[Z_1] = \begin{array}{c} \\ t_1 \\ t_2 \\ \vdots \\ t_{N_t} \end{array} \begin{array}{c} \begin{array}{cccc} x_1 & x_2 & \cdots & x_M \end{array} \\ \begin{bmatrix} p_{11} & p_{12} & \cdots & p_{1M} \\ p_{21} & p_{22} & & \vdots \\ \vdots & & \ddots & \vdots \\ p_{N_t 1} & \cdots & \cdots & p_{N_t M} \end{bmatrix} \end{array}. \tag{26}$$

Note that some zero-padding of $\boldsymbol{P}_{tx}$ in the x direction may be required to avoid spatial aliasing in the focused image [23]. The discrete Fourier transform of $\boldsymbol{P}_{tx}[Z_1]$ is also an N_t times M matrix, and we denote this matrix $\hat{\boldsymbol{P}}_{\omega k_x}[Z_1]$. The elements of $\hat{\boldsymbol{P}}_{\omega k_x}[Z_1]$ correspond to ω in the range $[-\pi f_s, \pi f_s]$, but only elements that correspond to the transducer passband are significantly different from zero. Because the frequency spectra of real valued signals are symmetric, we can also limit the processing to positive ω values. Denoting the upper and lower cutoff frequency for the transducer by $f_{\min}$ and $f_{\max}$, we define $\boldsymbol{P}_{\omega k_x}[Z_1]$ as the subset of $\hat{\boldsymbol{P}}_{\omega k_x}[Z_1]$ corresponding to $\omega \in 2\pi[f_{\min}, f_{\max}]$:

$$\boldsymbol{P}_{\omega k_x}[Z_1] = \begin{array}{c} \\ \omega_1 \\ \omega_2 \\ \vdots \\ \omega_{N_\omega} \end{array} \begin{array}{c} \begin{array}{cccc} k_{x1} & k_{x1} & \cdots & k_{xM} \end{array} \\ \begin{bmatrix} P_{11} & P_{12} & \cdots & P_{1M} \\ P_{21} & P_{22} & & \vdots \\ \vdots & & \ddots & \vdots \\ P_{N_\omega 1} & \cdots & \cdots & P_{N_\omega M} \end{bmatrix} \end{array}, \tag{27}$$

where $\omega_1 = 2\pi \left\lfloor N_t \frac{f_{\min}}{f_s} \right\rfloor$, $\omega_{N_\omega} = 2\pi \left\lceil N_t \frac{f_{\max}}{f_s} \right\rceil$, and the step size is $\Delta\omega = 2\pi f_s / N_t$. The relationship between N_ω and N_t is given by the ratio of transducer bandwidth to sampling frequency:

$$N_\omega / N_t \approx (f_{\max} - f_{\min})/f_s. \tag{28}$$

Also, assuming that the Fourier transform output is arranged so that the zero wavenumber is centered, and that M is even, the k_x wavenumbers are given by

$$\boldsymbol{k}_x = \frac{2\pi}{\Delta X \cdot M} \cdot [-M/2, -M/2+1, \cdots, 0, \cdots, M/2-1]. \tag{29}$$

B. Wave field extrapolation

We know from Eq. (18) and Eq. (19) that a wavefield at depth Z_l can be shifted to an arbitrary depth $Z_l + \Delta z$ within layer l by multiplication with a complex exponential $e^{ik_{zl}\Delta z}$, where k_{zl} is given by

$$k_{zl} = -\mathrm{sgn}(\omega) \cdot \sqrt{\frac{\omega^2}{\hat{c}_l^2} - k_x^2}. \tag{30}$$

The frequency-wavenumber spectrum should be limited to propagating waves, corresponding to real-valued k_{zl}, and this requirement is fulfilled as long as the square root argument of Eq. (30) is positive. All elements of $\boldsymbol{P}_{\omega k_x}$ for which $\frac{\omega^2}{\hat{c}_l^2} - k_x^2 < 0$ should therefore be set to zero.

Let $\boldsymbol{K}_{zl}$ be the discrete matrix representation of k_{zl}. It is an N_ω times M matrix given by

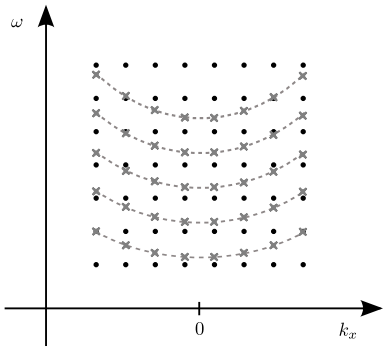

Figure 7: Interpolation points in $\omega - k_x$ domain

$$\boldsymbol{K}_{zl} = \begin{bmatrix} k_{zl}(\omega_1, k_{x1}) & \dots & k_{zl}(\omega_1, k_{xM}) \\ \vdots & \ddots & \vdots \\ k_{zl}(\omega_{N_\omega}, k_{x1}) & \dots & k_{zl}(\omega_{N_\omega}, k_{xM}) \end{bmatrix}. \quad (31)$$

The extrapolation from depth Z_l to depth $Z_l + \Delta z$ is performed with an entrywise multiplication:

$$\boldsymbol{P}_{\omega k_x}[Z_l + \Delta z] = \boldsymbol{P}_{\omega k_x}[Z_l] \circ \exp\left(i\boldsymbol{K}_{zl}\Delta z\right) \quad (32)$$

C. Stolt transformation of variables

We know from Section II-F that the transformation from the (ω, k_x) domain to the (k_z, k_x) domain is given by

$$P(k_z, k_x, Z_l) = A_l(k_z, k_x) \cdot P_l(\omega_l(k_z, k_x), k_x, Z_l) \quad (33)$$

where

$$A_l(k_z, k_x) = \frac{\hat{c}_l}{\sqrt{1 + \frac{k_x^2}{k_{zl}^2}}}, \quad \text{and} \quad (34)$$

$$\omega_l(k_z, k_x) = -\text{sgn}(k_{zl}) \cdot \hat{c}_l \sqrt{k_x^2 + k_{zl}^2} \quad (35)$$

The discrete version of $P(\omega, k_x, Z_l)$, $\boldsymbol{P}_{\omega k_x}[Z_l]$, is computed for a finite, equally spaced set of ω values. Similarly, the discrete version of $P(k_z, k_x, Z_l)$, denoted by $\boldsymbol{P}_{k_z k_x}[Z_l]$, should be computed for a equally spaced set of k_z. However, the mapping given by $\omega_l(k_z, k_x)$ does not in general coincide with the equispaced values of ω, and therefore a interpolation step is needed. The situation is illustrated in figure 7, where the original $\omega - k_x$ grid is indicated as black dots. For each discrete value of k_x, the spectrum has to be interpolated to a new set of ω values, indicated with gray crosses.

Using Eq. (35), we find that for a given k_{xj}, the ω values to be interpolated for are given by the vector

$$\boldsymbol{\omega}_l^{ip}(j) = \hat{c}_l \cdot \sqrt{k_{xj}^2 + \boldsymbol{k}_{zl}^2}, \quad (36)$$

where the sign function is omitted because only positive ω values are included in the processing. $\boldsymbol{k}_{zl}$ denotes the vector containing the discrete k_z values, and it is squared element by element. The interpolated values also have to be scaled according to Eq. (34), and the amplitude factors for k_{xj} are given by

$$\boldsymbol{a}_l(j) = \frac{\hat{c}_l}{\sqrt{1 + k_{xj}^2/\boldsymbol{k}_{zl}^2}}. \quad (37)$$

Assuming that all k_z values are negative, the $\boldsymbol{k}_{zl}$ vector is given by

$$\boldsymbol{k}_{z,l} = -\Delta k_{z,l} \cdot [0, 1, \dots, N_{k_z} - 1]^T. \quad (38)$$

$\Delta k_{z,l}$ is the step size between each value, and N_{k_z} is the total number of values, and these should be chosen to cover the range of possible k_z values and also avoid any aliasing. This is fulfilled if

$$\Delta k_{z,l} \leq \frac{2\pi}{\hat{c}_l} \cdot \frac{f_s}{N_t}, \quad (39)$$

and

$$N_{k_z} \geq \frac{2\pi f_{\max}/\hat{c}_l}{\Delta k_{z,l}}. \quad (40)$$

D. Algorithm description

Figure 8 illustrates the flow of the PSM and the MULOK algorithms, from the input ultrasonic data (denoted by $\boldsymbol{P}_{tx}[Z_1]$) to the focused image (denoted by $\boldsymbol{I}_{zx}$). $\boldsymbol{P}_{tx}[Z_1]$ is first Fourier transformed, and the elements corresponding to the transducer passband are extracted. Then, for each layer, the wavefield is multiplied with the phase factor $\exp\left(i\sum_{m=1}^{l-1}\boldsymbol{K}_{zm}d_m\right)$ to shift it from Z_1 down to the top of the layer l, given by Z_l. For the first layer, the phase factor is set equal to 1, resulting in zero phase shift. The shifted wavefield is a common starting point for both algorithms, and the subsequent steps for PSM and MULOK are shown on the left and the right side of the flowchart, respectively.

The PSM algorithm is based on forming an image line $\boldsymbol{i}(Z_l + \Delta z)$ for each depth to be imaged. The first operation is to compute $\boldsymbol{P}_{\omega k_x}[Z_l + \Delta z_l]$ by multiplying with the additional phase factor $\exp\left(i\boldsymbol{K}_{zl}\Delta z_l\right)$. An image line is then formed by summing over all ω and inverse Fourier transforming the resulting vector.

For the Stolt imaging algorithm, the next step after calculating $\boldsymbol{P}_{\omega k_x}[Z_l]$ is to interpolate from the original $\omega - k_x$ grid to the $k_x - k_z$ grid. This is done by looping through all k_z values, interpolating for each column of $\boldsymbol{P}_{\omega k_x}[Z_l]$ with the ω values given by the $\boldsymbol{\omega}_l^{ip}(j)$ vector, and multiplying with the $\boldsymbol{a}_l(j)$ vector. Only part of the result corresponds to z values within the layer, that is, $\Delta z \in [0, d_l]$. For each layer, this part is cut out and saved as the local image $\boldsymbol{I}_{zx}[l]$.

When all the layers have been processed, the subimages $\boldsymbol{I}_{zx}[l]$ are stacked on top of each other to form the complete image of all the layers.

E. Asymptotic complexity

Having defined both the PSM and the MULOK implementations, it is possible to study the computational complexity of the two. Big O notation is used to describe

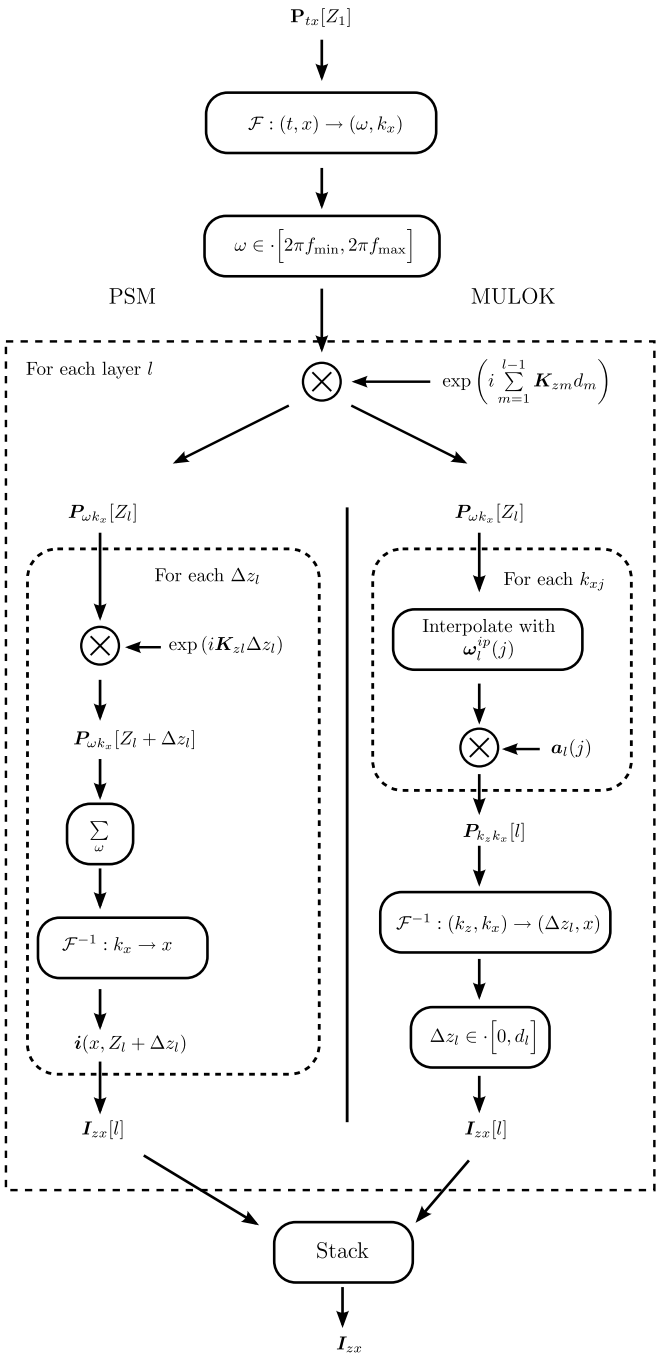

Figure 8: Flowchart for Stolt and Phase Shift algorithms

the growth rate of operations as function of the size of the input data. As described in Section D, the raw data $\boldsymbol{P}_{tx}[Z_1]$ is a N_t times M matrix, corresponding to N_t time samples and M measurement positions. After Fourier transforming the data, a N_ω times M submatrix of the result is extracted for use in the subsequent processing, where N_ω is proportional to N_t. The number of z lines for the PSM algorithm, denoted by N_z, and the number of k_z values for the MULOK algorithm, denoted by N_{k_z}, are also proportional to N_t. For the sake of asymptotic complexity analysis, we can ignore all such proportionality constants, and set $N_t = N_\omega = N_z = N_{k_z} = N$. The number of layers is denoted by L.

The initial Fourier transform, from (t, x) to (ω, k_x), is a two-dimensional transform with complexity $O(MN \log MN)$. The following multiplication with a phase factor to calculate $\boldsymbol{P}_{\omega k_x}[Z_l]$ is a entrywise multiplication that is performed $L - 1$ times. The complexity of this operation is thus $O(NML)$.

For the phase shift migration algorithm, the wave field is multiplied with yet another phase factor. This multiplication is performed N times, once for each image line, and thus the complexity for all image lines is $O(MN^2)$. The summation over ω is also perfomed N times, resulting in a total complexity of $O(MN^2)$. Finally, the last operation is the inverse Fourier transform of an M-length vector, which is $O(MN \log M)$. The complexities of the individual steps of the PSM algorithm are summarized in Table II.

Operation	Complexity
Initial Fourier transform	$O\big(MN \log MN\big)$
Phase shift to Z_l	$O(LMN)$
Phase shift to $Z_l + \Delta z_l$	$O(MN^2)$
Summation over ω	$O(MN^2)$
Inverse transform (k_x)	$O(MN \log M)$

Table II: Complexity for the individual steps of the PSM algorithm

For the MULOK algorithm, the calculation of $\boldsymbol{P}_{\omega k_x}[Z_l]$ is followed by an interpolation step. The complexity of this step depends on the type of interpolation utilized, but in this work, the following method was used: $\boldsymbol{P}_{\omega k_x}[Z_l]$ was first interpolated to a denser rectangular grid by inverse Fourier transforming, zeropadding, and Fourier transforming back again. This operation is $O(MN \log N)$. The final interpolation was subsequently performed by linear interpolation between points on this denser grid. This operation consists of a search to find the two closest ω values and calculating a weighted sum of P for these values, and the corresponding complexity is $O(MN \log N)$. Since the 2-D interpolation is performed once for each layer, the overall complexity is then $O(LMN \log N)$. Multiplication with the amplitude factors $\boldsymbol{a}_l(j)$ is $O(LMN)$, and the inverse Fourier transform to produce the image is $O(LMN \log MN)$. The complexities of the different steps of the MULOK algorithm are summarized in Table III.

Operation	Complexity
Initial Fourier transform	$O\big(MN \log MN\big)$
Phase shift to Z_l	$O(LMN)$
Interpolation from ω to k_z	$O(LMN \log N)$
Amplitude scaling	$O(LMN)$
Inverse Fourier transform	$O\big(LMN \cdot \log MN\big)$

Table III: Complexity of the individual steps of the MULOK algorithm

Acknowledgement

The authors would like to thank Prof. T. Stepinski for inviting M.H. Skjelvareid to the Signals and Systems Group at Uppsala University, where most of this research was carried out.

References

[1] J. B. Bednar, "A brief history of seismic migration," *Geophysics*, vol. 70, pp. 3MJ – 20MJ, 2005.

[2] R. H. Stolt, "Migration by Fourier transform," *Geophysics*, vol. 43, no. 1, pp. 23–48, February 1978.

[3] J. Gazdag, "Wave equation migration with the phase-shift method," *Geophysics*, vol. 43, no. 7, pp. 1342–1351, 1978.

[4] J. W. Goodman, *Introduction to Fourier Optics*, 2nd ed. McGraw-Hill, 1996.

[5] E. G. Williams, *Fourier Acoustics*. Academic Press, 1999.

[6] S. Doctor, T. Hall, and L. Reid, "SAFT - the evolution of a signal processing technology for ultrasonic testing," *NDT International*, vol. 19, no. 3, pp. 163–167, June 1986.

[7] K. Langenberg, M. Berger, T. Kreutter, K. Mayer, and V. Schmitz, "Synthetic aperture focusing technique signal processing," *NDT International*, vol. 19, no. 3, pp. 177–189, June 1986.

[8] K. Mayer, R. Marklein, K. Langenberg, and T. Kreutter, "Three-dimensional imaging system based on Fourier transform synthetic aperture focusing technique," *Ultrasonics*, vol. 28, pp. 241–255, July 1990.

[9] L. J. Busse, "Three-dimensional imaging using a frequency-domain synthetic aperture focusing technique," in *IEEE Trans. Ultrason., Ferroelectr., Freq. Control*, vol. 39, no. 2, March 1992.

[10] Y.-F. Chang and C.-C. Chern, "Frequency-wavenumber migration of ultrasonic data," *Journal of Nondestructive Evaluation*, vol. 19, no. 1, pp. 1–10, 2000.

[11] T. Stepinski, "An implementation of synthetic aperture focusing technique in frequency domain," *IEEE Trans. Ultrason., Ferroelectr., Freq. Control*, vol. 54, no. 7, pp. 1399–1408, July 2007.

[12] N. Pörtzgen, D. Gisolf, and G. Blacquière, "Inverse wave field extrapolation: A different NDI approach to imaging defects," *IEEE Trans. Ultrason., Ferroelectr., Freq. Control*, vol. 54, no. 1, pp. 118–127, January 2007.

[13] A. J. Hunter, B. W. Drinkwater, and P. D. Wilcox, "The wavenumber algorithm for full-matrix imaging using an ultrasonic array," *IEEE Trans. Ultrason., Ferroelectr., Freq. Control*, vol. 55, no. 11, pp. 2450–2462, November 2008.

[14] M. A. Haun, D. L. Jones, and W. D. O'Brien Jr., "Adaptive focusing through layered media using the geophysical "time migration" concept," in *2002 IEEE Ultrasonics Symposium*, vol. 2, 2002, pp. 1635 – 1638.

[15] M. H. Skjelvareid and Y. Birkelund, "Ultrasound imaging using multilayer synthetic aperture focusing," in *Proceedings of the ASME 2010 Pressure Vessels and Piping Division / K-PVP Conference*, 2010.

[16] T. Olofsson, "Phase shift migration for imaging layered object and objects immersed in water," submitted for publication in *IEEE Trans. Ultrason., Ferroelectr., Freq. Control*.

[17] Y. C. Kim, R. Gonzalez, and J. R. Berryhill, "Recursive wavenumber-frequency migration," *Geophysics*, vol. 54, no. 3, pp. 319–329, March 1989.

[18] J. F. Claerbout, *Imaging the Earth's Interior*. Blackwell Scientific Publications, 1985.

[19] G. M. Margrave, *Numerical Methods in Exploration Seismology - with algorithms in MATLAB*. University of Calgary, 2003.

[20] L. Brekhovskikh and O. Godin, *Acoustics of Layered Media I: Plane and Quasi-Plane Waves*, Springer Series on Wave Phenomena. Springer-Verlag, 1990.

[21] P. T. Gough and D. W. Hawkins, "Unified framework for modern synthetic aperture imaging algorithms," *Int. J. Imag. Syst. Tech*, vol. 8, no. 4, pp. 343–358, 1998.

[22] R. Lanari, "A new method for the compensation of the sar range cell migration based on the chirp z-transform," *IEEE Trans. Geosci. Remote Sens.*, vol. 33, no. 5, pp. 1296–1299, 1995.

[23] K. Gu, J. Wang, and J. Li, "Migration based sar imaging for ground penetrating radar systems," in *IEE Proceedings - Radar, Sonar and Navigation*, vol. 151, no. 5, October 2004.